Check for updates

Ultrafast laser surgery probe with a calcium fluoride miniaturized objective for bone ablation

KAUSHIK SUBRAMANIAN,[1,5] LIAM ANDRUS,[2,5] MICHAL PAWLOWSKI,[3] YE WANG,[3] TOMASZ TKACZYK,[3] AND ADELA BEN-YAKAR[1,2,4,*]

[1]*The University of Texas at Austin, Department of Mechanical Engineering, 204 East Dean Keeton Street, Stop C2200, Austin, Texas 78712, USA*

[2]*The University of Texas at Austin, Department of Biomedical Engineering, 107 West Dean Keeton Street, Stop C0800, Austin, Texas 78712, USA*

[3]*Rice University, Department of Bioengineering, 6100 Main Street, Houston, Texas 77005, USA*

[4]*The University of Texas at Austin, Department of Electrical and Computer Engineering, 2501 Speedway, Stop C0803, Austin, Texas 78712, USA*

[5]*These authors contributed equally to this work*

[*]ben-yakar@mail.utexas.edu

Abstract: We present a miniaturized ultrafast laser surgery probe with improved miniaturized optics to deliver higher peak powers and enable higher surgical speeds than previously possible. A custom-built miniaturized CaF_2 objective showed no evidence of the strong multiphoton absorption observed in our previous ZnS-based probe, enabling higher laser power delivery to the tissue surface for ablation. A Kagome fiber delivered ultrashort pulses from a high repetition rate fiber laser to the objective, producing a focal beam radius of 1.96 μm and covering a 90×90 μm^2 scan area. The probe delivered the maximum available fiber laser power, providing fluences >6 J/cm^2 at the tissue surface at 53% transmission efficiency. We characterized the probe's performance through a parametric ablation study on bovine cortical bone and defined optimal operating parameters for surgery using an experimental- and simulation-based approach. The entire opto-mechanical system, enclosed within a 5-mm diameter housing with a 2.6-mm diameter probe tip, achieved material removal rates >0.1 mm^3/min, however removal rates were ultimately limited by the available laser power. Towards a next generation surgery probe, we simulated maximum material removal rates when using a higher power fiber laser and found that removal rates >2 mm^3/min could be attained through appropriate selection of laser surgery parameters. With future development, the device presented here can serve as a precise surgical tool with clinically viable speeds for delicate applications such as spinal decompression surgeries.

1. Introduction

Ultrafast laser ablation is ideal for surgical procedures requiring precise tissue removal. For example, current spinal decompression (i.e., bone spur removal) surgeries suffer from a medley of complications, which arise primarily from the biting and cutting tools available to surgeons [1–4]. Unlike these mechanical tools, which require multiple extractions from the surgery space to remove the entire region of interest (ROI), laser-based tools could remove a bone spur during a single insertion, potentially reducing complication rates and improving clinical outcomes. Further, due to a high degree of spatial and thermal confinement, ultrafast laser ablation can achieve better surgical resolution than conventional lasers [5] to provide the utmost precision and safety during surgery in biologically sensitive regions such as the spine.

Although ultrafast lasers are routinely used for femtosecond laser assisted in-situ keratomileusis (fs-LASIK) and for cataract surgeries, clinical adoption has been largely restricted to ophthalmology, where easy access to the eyes facilitates direct, free space delivery of light. For surgical

applications in other areas of the body, a miniaturized delivery system must be developed. For example, prior research has explored ultrafast laser ablation of bone tissue [6–10], however clinical efficacy was restricted by the bulky free space optics used in these studies. Specifically, clinical adaptation of ultrafast laser tissue microsurgery requires miniaturized probes to provide access to restricted surgical sites in or on a patient.

Towards clinical acceptance of ultrafast laser surgery, various miniaturized surgical probes have been developed [11–15]. Specifically, our group has developed 4 generations of probes, progressively decreasing the cross-sectional diameter from 18 mm [11] to 5 mm [13,15] while delivering higher average powers using a photonic bandgap hollow-core photonic crystal fiber (HC-PCF) [13], and, more recently, a Kagome-type HC-PCF [15], coupled to a high repetition rate fiber laser. While the larger core of the Kagome fibers allowed delivery of higher pulse energies than the photonic bandgap fibers, their low numerical aperture (NA) required custom optics to enable moderate NA beam focusing (i.e., large demagnification) on the tissue surface for ablation [15]. We therefore designed and built a miniaturized objective consisting of two zinc sulfide (ZnS) lenses fabricated using diamond turning. However, transmission measurements revealed maximum deliverable laser pulse energy was limited by multiphoton absorption in the ZnS objective. Specifically, we observed three-photon absorption in ZnS when transmitting 803 nm, 1.5 ps pulses beyond a pulse energy of ~1.4 μJ (corresponding to an input peak power of ~0.8 MW and peak intensity of ~3.2 GW/cm^2 at the smallest spot size within the objective), gradually decreasing transmission efficiency and restricting the laser power delivered to the tissue surface.

As material removal rates are strongly tied to laser power delivery, in this paper, we present an improved ultrafast laser surgery probe with miniaturized calcium fluoride (CaF$_2$) optics to deliver higher laser peak powers to the tissue surface. The new CaF$_2$ objective exhibits negligible multiphoton absorption, enabling higher peak power pulse delivery while focusing over a larger ablation FOV when compared to our previous ZnS-based probe. To showcase the probe's surgical performance as a precise surgical method to remove bone spurs, we performed parametric ablation studies on bovine cortical bone. The experiments helped us to define optimal operating parameters for rapid bone ablation. Using these experimental findings and considering various limitations related to ultrafast laser-material interaction processes, we could determine the maximum material removal rates, *MRR*. Surgical speeds up to 2 mm^3/min should be achievable with a next generation ultrafast laser surgery probe built around a high power, high repetition rate fiber laser.

2. Experimental approach

2.1. Surgery probe design

An ultrafast laser surgical probe must meet multiple key requirements for clinical adoption. (1) Delivery of high average laser powers to provide clinically relevant material removal rates. (2) Beam focusing on the tissue surface to initiate ablation. (3) Beam steering of the focused spot over a large FOV to rapidly distribute the laser pulses arriving at high repetition rates. (4) Finally, a small form factor suitable for endoscopic use.

The ultrafast laser surgery probe, shown in Fig. 1(a), incorporated the same inline architecture presented in Subramanian *et al.* [15], while a custom miniaturized objective was designed using CaF$_2$ to enable high peak power pulse delivery. Calcium fluoride (CaF$_2$) is an optical material that can circumvent the power limiting behavior of ZnS that we observed in our previous studies, thanks to its small nonlinear absorption coefficients, high damage thresholds, low chromatic dispersion, and efficient transmission of NIR pulses [16–18]. Further, the low refractive index of CaF$_2$ removes the need for anti-reflection coatings, enabling easier objective fabrication. While an optical system fabricated from a lower refractive index material would require a more complicated optical design to provide similar performance as the ZnS probe, negligible

multiphoton absorption in CaF_2 should enable linear operation at higher peak intensities. Indeed, recent studies demonstrated linear transmission through a CaF_2 window when using 1035 nm, 300 fs pulses with peak intensities up to ~380 GW/cm^2 [18], approximately ~120 times higher than the linear transmission limit of ZnS at 776 nm [15].
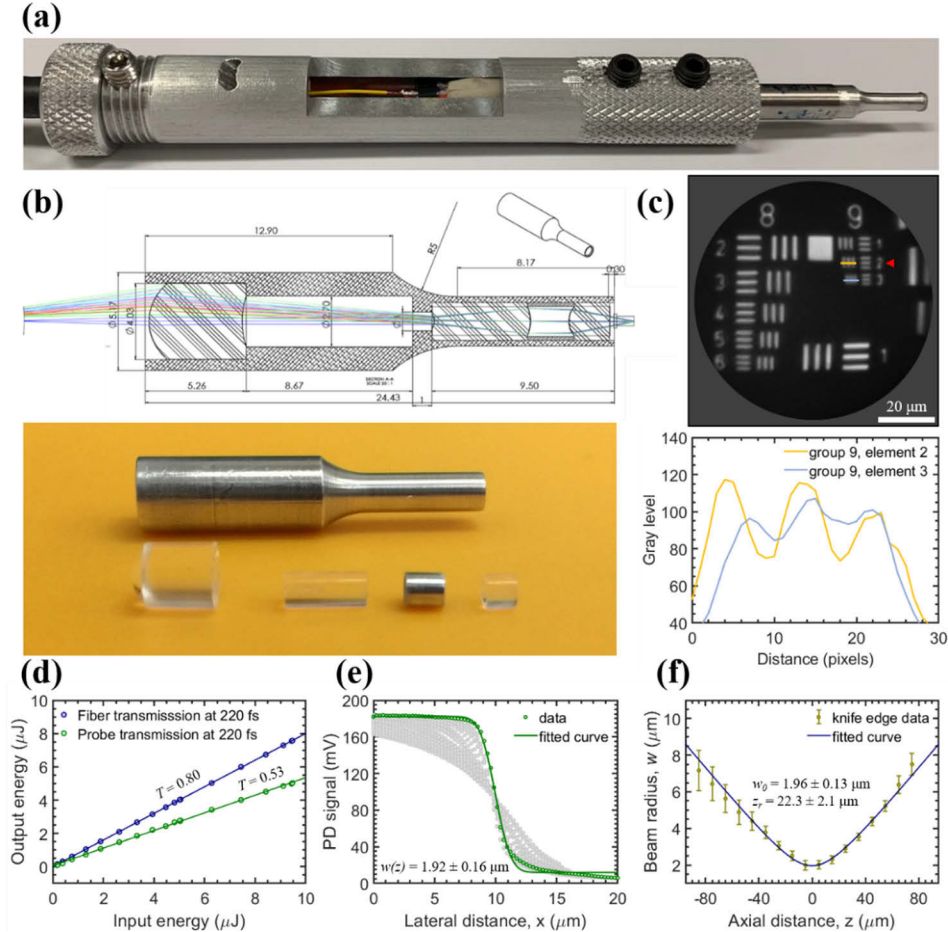
Fig. 1. Design and characterization of 5-mm surgical probe with a miniaturized CaF_2 objective. (a) Final probe assembly held within a ruggedized 14-mm housing. (b) Cross-sectional view of objective assembly. An optical ray trace depicting different launch angles from the fiber tip is superimposed. Lower image shows fabricated CaF_2 lenses alongside an objective housing with a 2.6-mm tapered tip. (c) USAF resolution target imaged with the miniaturized objective. The red arrow shows the minimum resolvable element in group 9. The plot below shows the line profile analysis results for the vertical elements in group 9. (d) Transmission efficiency (T) of 803 nm, 220 fs pulses through the Kagome fiber and final probe assembly. Transmission efficiencies were similar with the fiber laser (776 nm, 1.5 ps) used in probe characterization. (e) Knife-edge measurements with one of the smallest beam radius measurements highlighted. Data was fit to the edge spread function to determine spot size at each z-position. (f) Measured beam radii as a function of position along the optical axis as obtained from knife edge measurements in (e). Data was fit to Gaussian beam divergence equation to determine the $1/e^2$ spot size at the focal plane (w_0) and Rayleigh range (z_r). Uncertainty bars represent 95% confidence intervals for fit of each knife edge measurement to the edge spread function.

We used Zemax for design, optimization, and tolerance analysis of the miniaturized objective (Fig. 1(b)). The optical design was optimized for 776 nm wavelength, seawater immersion, and a NA >0.2 to avoid unwanted self-focusing effects during ablation [15]. Further, we sought to attain the largest possible FOV while maintaining a maximum lens clear aperture of ~4 mm to fit the final objective into a ~5 mm diameter housing. The tapered objective design reduced the distal probe tip to 2.6 mm, approximately 50% smaller than the ZnS probe, to provide a better line of vision for endoscopic use.

The designed CaF_2 objective had a nominal NA of 0.21 in seawater across a 90×90 μm^2 FOV, corresponding to ~11× demagnification of the ±500 μm fiber tip deflection. Table 1 shows the optical prescription for the miniaturized objective. Under paraxial approximation and considering Gaussian beam truncation effects, Zemax simulations estimated $1/e^2$ focal beam radii of 1.78 μm and 1.81 μm, with corresponding Rayleigh ranges of 12.83 μm and 13.26 μm, for focusing in seawater and air, respectively. A Strehl ratio of >0.96 indicated diffraction limited performance across the FOV. We fabricated lenses with a diamond turning lathe, integrated these optics into the hypodermic housing, and used stainless-steel spacers to set distances between each lens (Fig. 1(b)). The fabrication process of miniaturized CaF_2 lenses with similar dimensions as the lenses used in our objective is described in a recent publication by Jeon *et al*. [19]. A thin cover glass window at the objective tip protected the optical assembly against accidental scratches and sealed the system from contaminants. We initially assessed performance by imaging a 1951 USAF resolution target; the objective could resolve group 9, element 2, indicating diffraction-limited performance (Fig. 1(c)).

Table 1. Optical prescription data for the CaF$_2$ objective.

Surface	Radius (mm)	Thickness (mm)	Material	Semi-diameter (mm)	Conic
1	∞	0.900	Seawater	0.070	–
2	∞	0.150	BK7	0.248	–
3	∞	0.200	–	0.375	–
4	∞	2.124	CaF$_2$	0.429	–
5	-1.102	2.001	–	0.781	-0.638
6	1.916	5.000	CaF$_2$	0.758	–
7	0.579	10.003	–	0.369	-0.630
8	-4.832	4.852	CaF$_2$	1.332	4.402
9	-2.207	6.494	–	2.013	-0.872
10	6.670	–	–	0.739	–

The miniaturized objective was designed as a standalone opto-mechanical assembly, which allowed the probe to work with different objectives in a "plug-and-play" configuration. The Kagome fiber (0.019 NA, 45 μm core diameter, 26 μm mode-field-diameter, PMC-PL-780-UP, GLOphotonics) coupled laser light into the miniaturized objective. To provide beam steering, a 10 mm cantilevered section of the distal fiber tip was Lissajous scanned across the objective's back aperture using a piezo ceramic tube. The entire probe was integrated inside a ~5 mm stainless-steel hypodermic housing. We further integrated the opto-mechanical assembly into a ruggedized, pen-like mechanical housing (Fig. 1(a)). The 14 mm diameter stainless-steel casing protected all sensitive optical and electrical components and flexible plastic tubing was fixed to the metal housing using epoxy to protect the fiber against accidental breakage.

2.2. Experimental setup

We utilized the experimental setup described in [15] for probe characterization. We used two different laser systems: 1) A low repetition rate a Ti:sapphire regenerative amplifier (1 W, 803 nm,

220 fs, 1 kHz, Spectra Physics) for optical transmission measurements through the Kagome fiber and CaF_2 objective (where high peak powers were needed) and for measuring the uniformity of individual spot sizes during gold ablation studies. 2) A high repetition rate Er-doped fiber laser (0.5 W, 1552 nm, 600 fs, 303 kHz, frequency doubled to 776 nm, 1.5 ps, Discovery, Raydiance Inc.), which is required for clinically viable surgical speeds, for focal plane characterization and bone ablation studies.

2.3. Sample preparation

Multiple sample types were prepared to characterize the performance of the miniaturized probe. Samples used during gold ablation studies consisted of 15 nm thick gold films sputter-coated onto glass coverslips. For FOV curvature studies, we deposited 1 μm fluorescent beads (F8823, FluoSpheres, Thermo Fisher Scientific) onto a glass coverslip at 1 μL/mL concentration. For bone ablation studies, we purchased fresh flanken-cut bovine ribs from a local butcher. Prior to experimentation, we removed soft and connective tissues from the bone surface and glued the back-side of each sample to a glass coverslip for integration into our experimental setup.

3. Results and discussion

3.1. Optical performance characterization

We characterized transmission properties of the objective by using high peak power laser pulses from our regenerative amplifier system. We coupled light into the Kagome fiber using a 100 mm focal length plano-convex lens and measured fiber transmission and overall transmission of the entire probe when including the objective. The overall transmission efficiency of the probe was 53% (Fig. 1(d)). Importantly, this value was constant over a range of input peak powers up to ~40 MW (~120 GW/cm^2 within the objective), indicating negligible multiphoton absorption in the CaF_2 objective. This was a significant improvement over the ZnS probe, where we observed three-photon absorption at peak intensities $\geq$ 3.2 GW/cm^2 at 776 nm [15].

We measured the $1/e^2$ focal beam radius, w_0, and Rayleigh range, z_r, of the probe in air using a Foucault knife edge test (Fig. 1(e) – (f)). While the objective was designed for water immersion, the relatively low NA allowed for characterization in air without deteriorating the focusing conditions substantially. We determined $w_0 = 1.96 \pm 0.13$ μm (corresponding to an effective NA of 0.19) and $z_r = 22.3 \pm 2.1$ μm, respectively 8% and 68% larger than estimates obtained from Zemax. Deviations from design values may have been caused by slight misalignment of the fiber tip with the objective's conjugate plane.

We characterized the probe's FOV size by measuring the ablation spot sizes across the FOV during gold ablation studies. Our 1 kHz regenerative amplifier allowed us to measure individual ablation spot diameters at multiple locations across the ablation FOV. We observed sparsely distributed ablation spots across the FOV for increasing pulse energies, varying between 10–40 nJ. We observed uniform ablation spots across the design FOV of 90×90 $μm^2$ (Fig. 2(a)). While the ablation FOV extended to 130×130 $μm^2$ at the highest tested fluence, the smaller ablation spots beyond the design FOV border indicated possible beam truncation or field curvature.

Gold ablation experiments allowed a second measurement of w_0 by measuring the ablation spot diameter (D) as a function of pulse energy (E) and using the relation [20]:

$$D^2 = 2w_0^2 \ln\left(\frac{E}{E_{th}}\right), \tag{1}$$

where E_{th} is the single-pulse ablation threshold energy. We measured ablation spot diameters at the center of the FOV for a range of input pulse energies (Fig. 2(b)). A logarithmic curve fit of D^2 as a function of pulse energy yielded the radius of laser beam spot at the gold surface, $w_0 = 1.88 \pm 0.23$μm, matching closely with knife edge measurements of the spot size at the focal

(a)

(b)

(c)

(d)

(e)
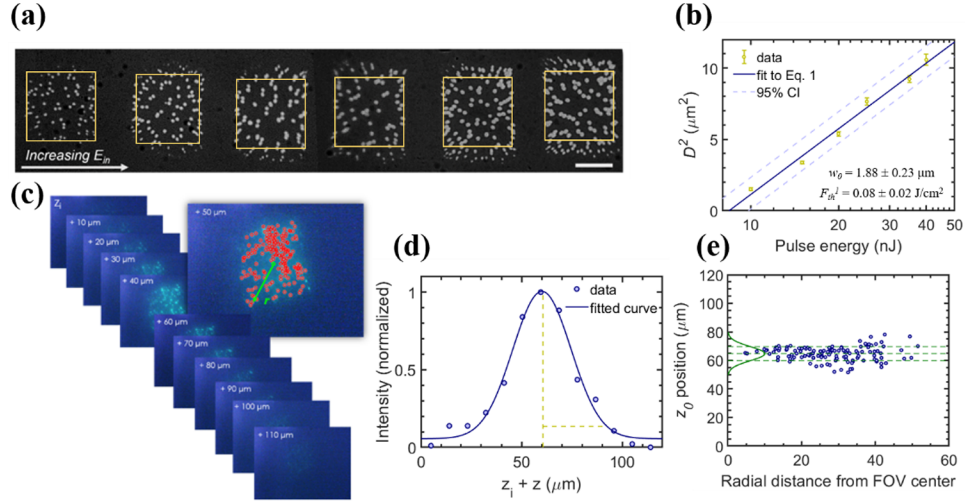
Fig. 2. Field-of-view characterization. (a) Gold ablation spots created with varying input pulse energies used to measure the laser spot size at the gold surface. Input pulse energies ranged from 10 to 40 nJ. The yellow squares represent the designed FOV of 90×90 μm². Scale bar is 50 μm. (b) Ablation spot diameter squared as a function of logarithmic pulse energy. Measured diameters represent the average of three ablation spots near the FOV center. Measurements were used to determine w_0 and F_{th}^1. Uncertainty bars of individual measurements represent 95% confidence intervals of the Gaussian beam fit to determine D^2, and the dotted lines represent 95% confidence intervals for the fit of data to Eq. (1). (c) Two-photon fluorescence images of polystyrene beads used to estimate FOV curvature. Measurements were initiated at some pre-focal z-position (z_i) with subsequent images taken every 10 μm through the focal plane of the probe. Inset shows a magnified $z_i + 50$ μm section, with bead positions highlighted. (d) Fluorescence intensity of a single bead tracked along the 13 z-planes shown in (c), with fit to Gaussian beam equation (Eq. (2)). The vertical line denotes the focal plane position ($z_0 \approx 60$μm) and the horizontal line denotes the $1/e^2$ width ($w_z \approx 29$μm). (e) Focal plane positions of all beads as a function distance from FOV center. The focal plane position of all beads lies within the Rayleigh range of the probe and does not show any radial dependence, implying negligible FOV curvature or astigmatism. Uncertainty bars for individual z_0 values were omitted for clarity.

plane. The measured $E_{th} = 8.5 \pm 1.6$ nJ corresponded to a single-pulse threshold fluence of $F_{th}^1 = 0.08 \pm 0.02$ J/cm² which compared favorably to previous studies [21,22].

We then characterized the probe's FOV curvature using a technique outlined in [23,24]. Briefly, we acquired two-photon fluorescence images of a monolayer of 1 μm fluorescent beads as they were scanned through the probe's focus and analyzed images to extract the $1/e^2$ axial fluorescence intensity profile width, w_z, at multiple locations across the FOV (Fig. 2(c) – (d)). The fluorescence intensity of each bead was tracked across multiple z-planes to estimate the axial location of the maximum fluorescence intensity, I_0, by fitting data to:

$$\frac{I(z)}{I_0} = \exp\left(\frac{-2(z - z_0)^2}{w_z^2}\right), \tag{2}$$

where z_0 is the z-position of each bead corresponding to I_0, i.e. the axial location of the focus at a single x-y location within the FOV. For a given NA, w_z is defined as [25]:

$$w_z = 0.532\lambda \left[\frac{1}{n - \sqrt{n^2 - NA^2}}\right], \tag{3}$$

where n is the refractive index of the medium, in our case air ($n = 1$). We determined $w_z = 26.8 \pm 3.4\mu m$, agreeing with the theoretical estimate of $w_z = 23.9\mu m$ obtained for the measured effective NA of 0.19. We then estimated the z_0 position of each bead relative to the FOV center. Our analysis revealed no discernable FOV curvature (Fig. 2(e)); z_0 of each bead lies within the measured Rayleigh range of the beam focus, with a 2σ variation of 9.4 μm. Our analysis showed no overarching trends with respect to radial distance from the FOV center, indicating that the focal plane was flat to within ~6°. Results indicated telecentric operation, with constant NA/magnification across the ablation FOV. In summary, the probe closely matched predicted design values. Pertinent metrics are summarized in Table 2.

Table 2. System parameters of surgical probe in air.

Piezo-fiber resonance frequencies	1.187 kHz and 1.203 kHz
Focal beam radius	1.96 ± 0.13 μm
Fiber scanning range	1×1 mm^2
Field-of-view	90×90 μm^2
Effective Numerical Aperture	0.19
Demagnification	$11\times$

### 3.2. Bone ablation and material removal rate measurements

We performed surgery on cortical bone samples to assess tissue ablation properties of the probe. We placed samples on a three-axis stage perpendicular to the probe and identified the focal plane-bone surface interface by axially translating bone samples towards the probe tip until ablation was detected visually. We then laterally offset the samples ~1 mm to avoid beginning experiments within the ablation crater produced during initial alignment. To measure the probe's ablation performance, we created ablation trenches on the bone surface by translating samples at different speeds (1–4 mm/s) while using multiple laser fluences (1.6–6.6 J/cm^2), and FOV scan widths (30, 66, and 92 μm). While no debris (ablation plume residue) was ever observed on the probe tip, we cleaned the probe with a lens cleaning solution after every ablation experiment. In all, a minimum of 3 ablation trenches were created for each parameter set.

Ablation trench depths and widths were analyzed using an optical profilometer (Wyko NT9100, Veeco Instruments) (Fig. 3). Figure 3(a) shows an example profilometry image of a single ablation trench, and Fig. 3(b) shows a single cross section (y-z plane) of the trench shown in Fig. 3(a). We manually selected the surgical ROI and determined trench depths (deepest z-position), $h_a(x)$, and full-width half maximum widths, $w_{FHWM}(x)$, at multiple trench cross sections (i.e., multiple y-z planes within the surgical ROI) using a prominence-based peak finding algorithm (Fig. 3(c) – (d)).

To estimate the ablation threshold fluence of the bovine cortical bone used in our experiments, we assessed the logarithmic dependence of ablation rate, d, on average laser fluence, F_{av}, according to [20,26,27]:

$$d = \alpha_{eff}^{-1} \ln\left(\frac{F_{av}}{F_{th}^N}\right), \tag{4}$$

where α_{eff}^{-1} is effective penetration depth defined by Beer-Lambert's law and F_{th}^N is the average fluence threshold when considering incubation. Incubation refers to the decreased fluence thresholds observed when ablating a material with a train of pulses. This effect is typically attributed to microscopic defects created on the sample surface by the first few initial pulses which provide increased energy absorption for successive pulses, leading to ablation at fluences below the single-pulse fluence threshold. Considering incubation effects, the ablation depth, h_a,

(a)

(b)

(c)

(d)
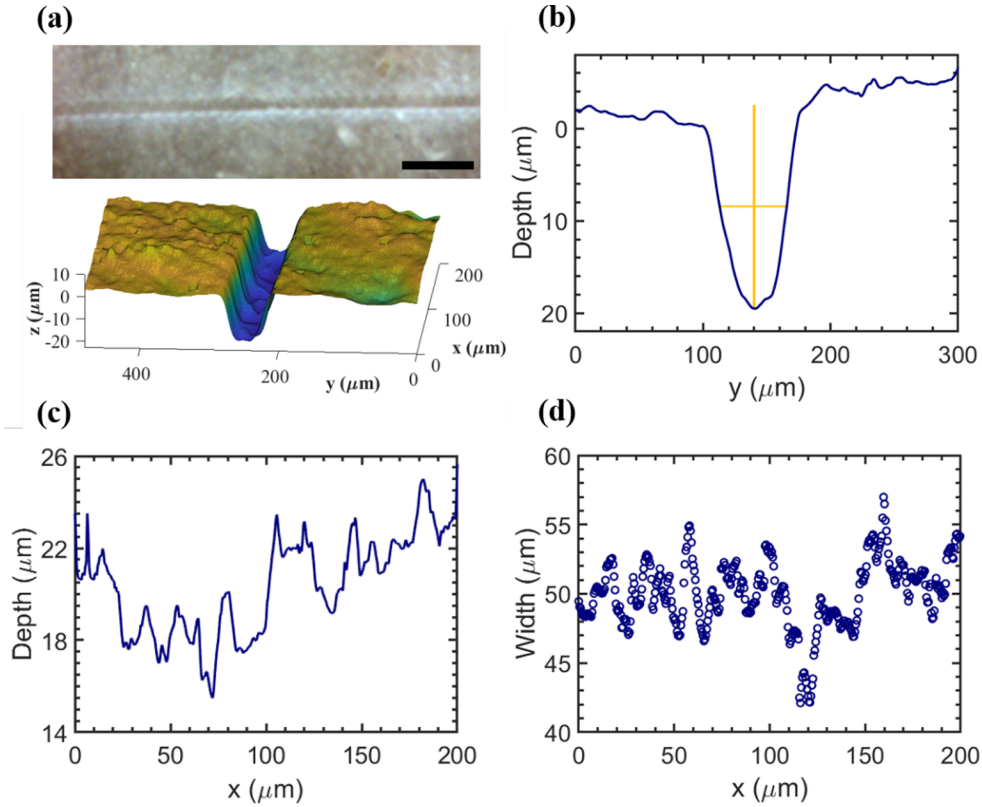
Fig. 3. Representative analysis of single ablation trench. (a) Top image shows an ablation trench created with 92 μm FOV scan width, 1 mm/s translation speed, and average fluence of 6.6 J/cm^2. Scale bar is 400 μm. Lower image shows a 3D rendering of the trench acquired with the profilometer after Gaussian smoothing. (b) An example cross section (y-z plane) of trench shown in (a). A prominence-based peak finding algorithm estimates trench depth ($h_a(x)$, vertical yellow line) and width ($w_{FWHM}(x)$, horizontal yellow line). (c) Trench depths for each cross section of trench shown in (a). (d) Trench widths for each cross section of trench shown in (a).

depends on the number of pulses incident on the sample surface [20,28–30]:

$$h_a = d(N - N_{th}),\qquad(5)$$

where N_{th} is the minimum number of pulses needed to initiate ablation. As we used fluences which exceeded the expected damage threshold of bone (1–3 J/cm^2), we assumed $N_{th} \approx 0$. Combining Eq. (4) and Eq. (5), h_a can be written as:

$$h_a = N\alpha_{eff}^{-1} \ln\left(\frac{F_{av}}{F_{th}^N}\right).\qquad(6)$$

We determined α_{eff}^{-1} and F_{th}^N by measuring the average ablation depth, h_a, along the mid-plane of each trench for ablation at different F_{av} (Fig. 4(a)). Due to the nonuniformity of Lissajous scanning, we expected nonuniform ablation depths as the number of overlapping pulses varies across the trench. We used a Lissajous scanning simulation [13,15] to estimate the average number of overlapping pulses along the trench mid-plane, N. The linear dependence of h_a on N

and $\ln(F_{av})$ (Eq. (6)) is only valid when the combination of N and F_{av} leads to shallow ablation depths, i.e. $h_a \leq 2z_r$. As this is the case for the data shown in Fig. 4(a), the slope of the linear relation between h_a and the logarithmic fluence gives $N\alpha_{eff}^{-1}$, while the intercept-to-slope ratio gives F_{th}^N. Using N predicted by Lissajous scan simulations, we estimated α_{eff}^{-1} and F_{th}^N for two different translation speeds (Table 3) We see good agreement between measured α_{eff}^{-1} values and previously reported α_{eff}^{-1} in dentin and porcine cortical bone [6,8].
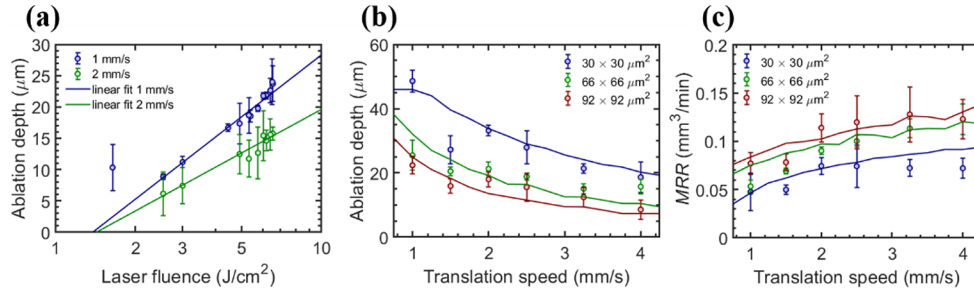
Fig. 4. Ablation performance of surgical probe. (a) Logarithmic dependence of average ablation depth (h_a) on average laser fluence (F_{av}) for two translation speeds at 92 μm FOV scan width. (b) Measured ablation depths (h_a) for multiple FOV scan widths and translation speeds at the maximum available average laser fluence of 6.6 J/cm^2. Theoretical ablation depths (h_{a0}) agreed well with experimental measurements. (c) Measured material removal rates (*MRR*) for multiple FOV scan widths and translation speeds. Theoretical material removal rates (*MRR$_0$*) agreed well with experimental measurements. Each data point in (a – c) represents the average of ≥ 3 ablation depth/width measurements and uncertainty bars in represent 95% confidence intervals.

Table 3. Summary of bone ablation parameters that are extracted from linear fits of average ablation depth (h_a) and logarithm of average fluence (F_{av}) for two translation speeds (v_x) for data presented in Fig. (4)a. The table summarizes the estimated average number of laser pulses along the trench mid-plane (N), effective penetration depth (α_{eff}^{-1}), multi-pulse ablation threshold (F_{th}^N), and single-pulse ablation threshold (F_{th}^1). Uncertainties are based on the standard errors of the slopes and y-intercepts.

v_x(mm/s)	N (pulses)	α_{eff}^{-1} (μm)	F_{th}^N (J/cm^2)	F_{th}^1 (J/cm^2)
1	25.83	0.55 ± 0.05	1.38 ± 0.18	1.98 ± 0.24
2	12.94	0.78 ± 0.07	1.43 ± 0.29	1.89 ± 0.38

We also determined single-pulse ablation thresholds (F_{th}^1) for both datasets by taking into account the incubation effect, which has been previously quantified by a power-law relationship [29]:

$$F_{th}^N = F_{th}^1 N^{\xi-1} \tag{7}$$

Here ξ is the incubation coefficient, which previous studies have estimated to be $\xi \approx 0.89$ for bone [9]. Both F_{th}^1 and F_{th}^N values were consistent between data sets and agreed with previously reported values for bovine cortical bone within 25% [31,32].

We used the ablation parameters shown in Table 3 and N values predicted by Lissajous simulations to infer ablation depths at other FOV scan widths and translation speeds (Fig. 4(b)). We found the measured penetration depth of $\alpha_{eff}^{-1} = 0.78 \pm 0.07$ μm produced the best fits for

our data. In our simulations, we determined the theoretical average ablation depths, h_{a0}, and multi-pulse ablation thresholds, F_{th0}^N, along the trench mid-plane using simulated N values and Eqs. (6) and (7), respectively. We assumed fluence threshold reduction due to incubation to be significant only within the first 20 overlapping pulses (i.e., $F_{th0}^N \geq F_{th0}^{N=20}$) [33]. For 20 overlapping pulses, $F_{th0}^{N=20} \approx 1.36$ J/cm² according to Eq. (7), agreeing well with experimental F_{th}^N values shown in Table 3. Further, we considered fluence variation across the ablation depth to account for beam divergence, limiting the maximum depth to a threshold range, $z_{th} = 2z_r\sqrt{(w_{th}/w_0)^2 - 1}$, where w_{th} is the $1/e^2$ beam radius along the optical axis where $F_{av} = F_{th}^1$. Simulated ablation depths, h_{a0}, agreed well with experimental measurements.

We used the profilometry data to estimate the average material removal rate, *MRR*, of the surgical probe (Fig. 4(c)). As ablation trenches were not well approximated by a rectangular cross section, the average trench widths predicted by our peak finding algorithm, w_{FWHM}, were not a reliable estimate of the trench width. Instead, we initially calculated the area of each cross section by manually selecting trench boundaries and integrated over this width using the *trapz* function in MATLAB. To estimate *MRR*, we multiplied the average cross-sectional area of multiple ablation trenches by translation speed, v_x. While providing the most accurate way for estimating *MRR*, this method was time intensive and computationally expensive. Instead, we found that approximating trenches as a trapezoidal volume of depth h_a, surface width $2w_{FWHM}$, and base width $0.25w_{FWHM}$:

$$MRR = \frac{9}{8}h_a w_{FWHM} v_x, \tag{8}$$

produced *MRR* estimates which agreed within 5% with the integration method values. At low speeds, we observed relatively higher *MRR* for larger FOV scan widths, which agreed with our simulations. This can be explained by the fact that, after a series of overlapping pulses produced an ablation depth equal to the threshold range, z_{th}, the remaining pulses are "wasted", as they do not contribute to material removal. Larger scanning widths dictated lower numbers of overlapping pulses and produced ablation depths which never approached z_{th}, even when slowly translating the probe. With faster translation speeds and/or large FOV scan widths (lower N), we would expect every pulse to contribute to material removal. Indeed, we observed asymptotic behavior in *MRR* measurements as translation speeds were increased for the two largest FOV scan widths. We determined a maximum *MRR* = 0.13 ± 0.03 mm³/min using a 4 mm/s translation speed, 92 μm FOV scan width, and the maximum available laser fluence of 6.6 J/cm². The material removal efficiency (*MRR* per watt) of our probe is 0.54 mm³/min/W, which is similar to 0.65 mm³/min/W measured in our ZnS-based probe [15].

We simulated theoretical material removal rate, MRR_0, to understand how our system compares to the expected performance. Using N predicted from Lissajous simulations, we calculated MRR_0 using Eq. (8), replacing the measured values (F_{th}^N, h_a, $2w_{FWHM}$) with theoretical ones (F_{th0}^N, h_{a0}, FOV scan width). Simulations indicated depth limiting behavior when many overlapping pulses per spot produced ablation depths $h_{a0} \approx z_{th}$, agreeing with the relatively smaller *MRR* measured for 30 μm and 66 μm FOV scan widths at translation speeds < 2 mm/s (Fig. 4(c)). For faster translation speeds, lower N resulted in higher MRR_0 values, as expected. For the current surgical probe, the simulated maximum material removal rate, MRR_0 = 0.13 mm³/min, agreed with the maximum measured *MRR*. Further, we calculated MRR_0 = 0.05 mm³/min for a 30 μm FOV scan width and 1 mm/s translation speed, representing the worst tested parameter set and matching closely with experimentally measured *MRR*.

3.3.   *Theoretical maximum material removal rates for an ultrafast laser surgery probe*

Achieving high material removal rates requires a high average power, high repetition rate laser source, such as our recently purchased Yb-doped fiber laser (40 W, 40 μJ max, λ = 1035 nm, 300

fs – 10 ps, 10 kHz – 50 MHz, Monaco, Coherent Inc.). When using miniaturized probes which focus ultrashort laser pulses onto the tissue surface through a liquid based environment, the laser parameters need to be carefully chosen to avoid certain nonlinear ultrafast laser processes and to achieve optimal surgical performance. In this section, we consider these processes and calculate the maximum material removal rates that can potentially be achieved using an ultrafast laser surgery probe.

As described in previous sections, lens materials need to be carefully selected when delivering high peak power ultrashort pulses for ablation. For example, a miniaturized ZnS objective, such as the one described in [15], will exhibit similar power-limiting behavior at 1035 nm. Using the experimental setup described in [18], open aperture z-scans of a ZnS window revealed a three photon absorption coefficient of $\alpha_3 \approx 1.5 \pm 0.4 \times 10^{-27}$ m^3/W^2, similar to previously reported values at 780 nm [34,35]. On the other hand, no nonlinear absorption was detected in a CaF$_2$ window when using 5× higher peak intensities in the same open aperture z-scan setup. Thus, a miniaturized CaF$_2$ objective should provide improved high pulse energy delivery at 1035 nm, similar to results shown in Fig. 1(d). When designing a next-generation CaF$_2$ probe around our 1035 nm fiber laser, careful optimization of various parameters such as average/peak power, laser repetition rate, translation speed, FOV, and focal beam size is needed to achieve maximum *MRR*. In the following sections, we simulate an optimal parameter space for such a system.

Generally speaking, high average powers are required to maximize *MRR*. Average powers can be increased by either increasing the number of laser pulses deposited per unit time and/or by increasing the pulse energies. We could increase pulse deposition rates by increasing the laser repetition rate, although high repetition rates without fast scanning may lead to unwanted pulse-to-pulse effects. As reviewed by Vogel *et al*., plasma-mediated cavitation is the dominant mechanism of tissue ablation when using femtosecond laser pulses at repetition rates below 1 MHz [5,36]. At fluences slightly above the threshold for optical breakdown, transient bubbles with lifetimes of a few hundred nanoseconds to a few microseconds may be created during the ablation process. For repetition rates above 1 MHz (< 1 µs pulse-to-pulse separation), bubbles formed by the first few consecutively overlapping pulses may shield later pulses, causing a reduction in ablation efficiency. Further, tissue ablation with high repetition rate lasers may lead to extensive heating and subsequent thermal damage of the targeted region, reducing the achievable precision. Thus, here we only consider laser repetition rates ≤ 1 MHz in our *MRR* simulations. This is a conservative upper limit for usable laser repetition rates, as rapid beam scanning over an ablation FOV should limit the number of consecutively overlapping pulses and therefore reduce the probability of bubble shielding and heat accumulation.

Alternatively, average powers can be increased with higher energy pulses as long as peak powers are below the critical peak power for self-focusing in the liquid media above the tissue surface, P_{crit}. Here, we assume P_{crit} is the limiting factor for peak power delivery, as P_{crit} is lower than the critical power for self-focusing in the Kagome fiber and the CaF$_2$ lenses. At peak powers beyond P_{crit}, self-focusing will prematurely collapse the beam, leading to focusing/bubble formation in the liquid media above the tissue surface. Thus, for a given pulse width, τ, and focal plane fluence, F_{av}, P_{crit} defines the minimum NA required to avoid the deleterious effects of self-focusing. Specifically, we need to determine the minimum NA which ensures $P_{peak} < P_{crit}$, where $P_{peak} = 0.88E/\tau$ is the peak power for a sech^2 pulse [37]. The critical peak power for self-focusing is defined as [38]:

$$P_{crit} = \frac{3.77\lambda^2}{8\pi n_0 n_2}. \tag{9}$$

Here, n_0 and n_2 are the linear and nonlinear refractive indices We estimated the collapse distance for a Gaussian beam focused using a lens with focal length f, z'_{sf} [39]:

$$z'_{sf} = \frac{z_{sf}f}{z_{sf} + f}, \tag{10}$$

where z_{sf} is the self-focusing collapse distance for a collimated Gaussian beam as defined by Marburger [38]. For $P_{peak} = P_{crit}$, $z_{sf} = \infty$, there is no self-focusing induced focal plane shift and therefore $z'_{sf} = f$. For saline, as representative of the liquid media, we calculated $P_{crit} \approx 3$ MW, assuming $n_0 = 1.33$ and $n_2 = 4.1 \times 10^{-7}$ cm^2/GW [38]. For 1.5 ps pulses, we can use ~5 μJ pulse energies (~5 W average power at 1 MHz) while $P_{peak} < P_{crit}$. A pulse width of 1.5 ps should be appropriate for ultrafast laser ablation with a next-generation probe, as ablation trenches created with the current probe and the 1.5 ps Er-doped fiber laser showed no evidence of thermal damage. Figure 5(a) presents the self-focusing collapse distance as a function of NA for different average fluences normalized to the experimentally measured single pulse fluence threshold, $F_{th}^1 = 1.89$ J/cm^2. Thus, we can determine the minimum NA required to ensure $P_{peak} < P_{crit}$ for a desired input fluence.
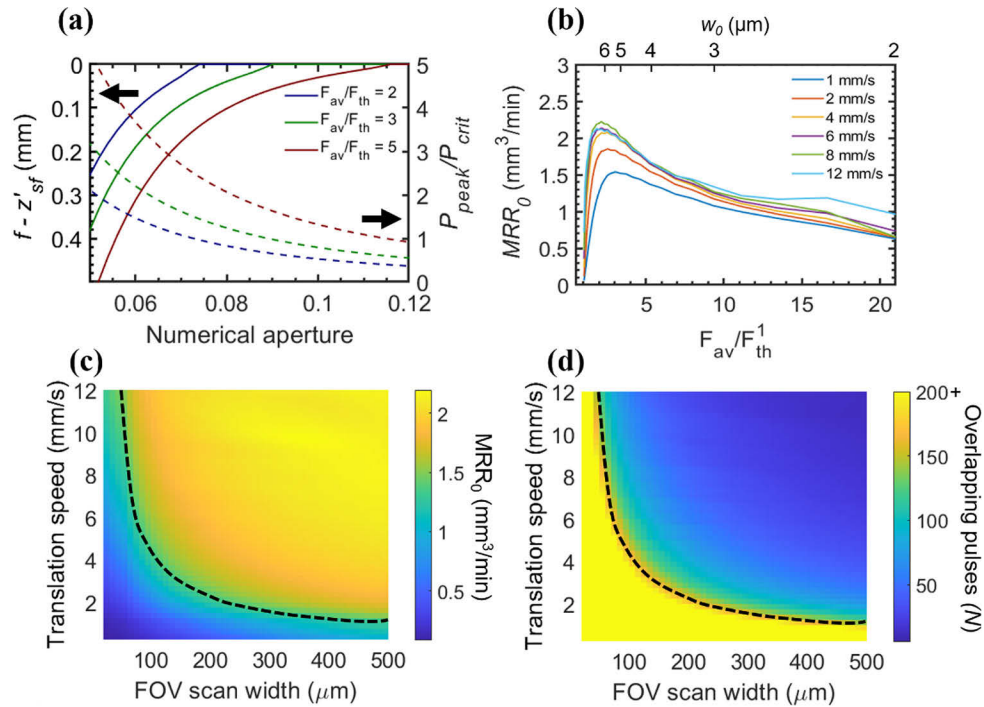
Fig. 5. Simulation results for next generation surgical probe. (a) Self-focusing collapse distances in saline (z'_{sf}) and peak power ratios (P_{peak}/P_{crit}) vs. numerical aperture (NA) for a Gaussian beam focused with a 3 mm focal length lens (and a varying input beam size). Solid lines represent $f - z'_{sf}$ for a range of fluence ratios (F_{av}/F_{th}^1, $F_{th}^1 = 1.89$ J/cm^2, left axis). Dashed lines are corresponding peak power ratios (P_{peak}/P_{crit}, right axis). (b) Theoretical material removal rate (MRR_0) vs. F_{av}/F_{th}^1 when using 1.5 ps, 5 μJ pulses at 1 MHz repetition rate (5 W average power). Fluence was varied by adjusting focal beam radii. Maximum MRR_0 occurs when input fluences are ~2–3 times the fluence threshold. Each curve in (b) represents MRR_0 for a single translation speed and a constant 500 μm FOV scan width. (c) MRR_0 and (d) N for multiple FOV scan widths and translation speeds when $F_{av} \approx 2.5F_{th}^1$. Focal beam radius, repetition rate, pulse width, and average power were 5.8 μm, 1 MHz, 1.5 ps, 5 W, respectively. The FOV scan width/translation speed combinations beyond the dashed lines in (c) and (d) correspond to ablation depths less than the threshold range (i.e., $h_a < z_{th}$) indicating all pulses contribute to the ablation process.

With maximum usable laser powers and minimum NA specified by our self-focusing calculations, we then determined the average laser fluences which produced the highest theoretical material removal rate, MRR_0 (Fig. 5(b)). Here, we calculated MRR_0 using the methodology described in section 3.2 for a 500 μm FOV scan width and multiple translation speeds. We found that focal plane fluences approximately 2–3 times the single-pulse ablation threshold, $F_{av} \approx 2F_{th}^1 - 3F_{th}^1$, produced the largest MRR_0, as this provided an optimal compromise between N and F_{av}. We confirmed this result by rerunning simulations at a range of pulse energy/laser repetition rate combinations (5 μJ/500 kHz, 2 μJ/1 MHz, 5 μJ/10 MHz), and various FOV scan widths and translation speeds. For 5 μJ pulse energies, $F_{av} \approx 2F_{th}^1 - 3F_{th}^1$ can be realized with a spot size of $w_0 \approx 5 - 6$μm, assuming a beam truncation ratio of 1 [40].

We then studied which FOV scan width and translation speed combinations produced the highest overall MRR_0 (Fig. 5(c)). The simulations showed that a maximum MRR_0 = 2.32 mm³/min can be achieved using a 350 μm FOV scan width and 10.25 mm/s translation speed. This value is ~18 times higher than the MRR measured with the probe described in this study. Further, the average power of 5 W assumed in our simulations is ~21 times larger than what was available (0.24 W delivered to tissue) in our current setup, suggesting that an approximately linear relationship exists between maximum material removal rates and deliverable laser power. Importantly, simulated material removal rates were approximately constant over a large scanning rate range, allowing for flexibility during surgery.

To further increase the surgical speed of a miniaturized probe, we could use pulses up to 10 ps to achieve higher pulse energies/average powers while avoiding the critical peak power limit for self-focusing. For example, we could deliver 20 W by using 6 ps, 20 μJ pulses at 1 MHz while maintaining $P_{peak} < P_{crit}$. In this case, the increased threshold range, z_{th}, of such a system may lead to bubble formation in the liquid media above the tissue surface, limiting ablation efficiencies.

A more feasible way to increase average powers would be to use a fiber bundle surgery probe that can simultaneously ablate multiple spots on the tissue surface. For example, 4 fibers can deliver 4 times higher average powers while avoiding the limitations of high peak intensities when using a single fiber. Such a configuration may consist of a piezo-scanned fiber bundle and a miniaturized objective to deliver multiple focused spots to the tissue surface. Thus, MRR up to 9 mm³/min (MRR_0 = 2.32 mm³/min for a single fiber delivering 5W, Fig. 5(c)) could be achieved while limiting the power delivered by a single laser beam.

3.4. Challenges in the clinical implementation of ultrafast laser surgery probes

In the clinic, handheld operation may be challenging, as the distance from the probe tip to the tissue surface needs to be tightly controlled to ensure ablation of the targeted region. For example, the focal plane of the probe described in Fig. 5(c) would need to be held ±125 μm from the tissue surface to maintain fluences above threshold. Thus, robotic manipulation may be necessary for clinical use. In this case, large tissue volumes could be removed in a stepwise fashion, where the ablation FOV is repositioned towards the target after a lateral scan removes a thin tissue layer.

Additionally, the probe tip will likely be immersed in blood during surgery. While absorption and scattering coefficients of blood are low at 1035 nm, attenuation of laser power may need to be considered for *in vivo* use. Sterilization will be required to use the probe for multiple surgeries. The potentially low melting point of the epoxy used in the probe assembly may prove problematic during autoclave sterilization, however heat resistance epoxies are available if this proves to be an issue. Further, other sterilization techniques (EtO, Gamma irradiation) may be used in lieu of autoclave sterilization.

As surgical laser systems would not require multiple extractions from the surgery site during spinal decompression, they may provide an inherent advantage over mechanical tools in terms of complication rates and total surgery times. According to Dr. Eeric Truumees, an orthopedic

surgeon and Professor of Surgery at the Dell Medical School, "removal of a single bone spur during a lumbar laminectomy typically takes 20–40 minutes when using mechanical tools, setup time excluded" [41]. Further, Dr. Truumees estimated an average bone spur length of 1–3 mm. Considering the maximum theoretical material removal rate for a 5 W ultrafast laser surgery probe (MRR_0 = 2.32 mm^3/min, Fig. 5(c)), a 3-mm thick bone spur could be removed in less than 2 minutes by ablating a 0.5-mm wide and 3-mm deep trench (a 4.5 mm^3 volume). While conventional laser surgery systems can achieve higher material removal rates [42–44], these systems are not used in biologically sensitive regions such as the spine due to the potential for accidental thermal damage beyond the surgical ROI. Thanks to its high spatial and thermal confinement, ultrafast laser surgery may safely and rapidly remove bone spurs while limiting the potential complications and extended surgery times associated with conventional laser surgery and traditional mechanical removal techniques.

4. Conclusions

We presented an ultrafast laser surgery probe with new CaF$_2$ optics to overcome the nonlinear absorption effects observed in our previous ZnS-based probe. A custom miniaturized CaF$_2$ objective produced a 1.96 μm focal beam radius, approximately 13% smaller than the spot size attained with our previous ZnS-based probe. Gold ablation studies revealed negligible variance in ablation crater diameters across a 90×90 μm^2 FOV, and two-photon fluorescence imaging studies showed minimal FOV curvature, indicating uniform energy distribution across a flat surgical ROI. Importantly, due to weak multiphoton absorption in the CaF$_2$ objective, we could deliver at least ~37× higher peak intensities than was possible with the ZnS probe, providing the possibility to achieve high *MRR*. The probe allowed a single mechanical body to work with multiple objectives, and this "plug-and-play" configuration should allow flexibility for a variety of surgical procedures.

The surgical performance of the probe was characterized through parametric ablation studies on excised bone tissue samples. Measured ablation rates and fluence thresholds of bovine cortical bone compared favorably with previously reported values for similar hard tissues. Measured material removal rates compared well with simulations which indicated that higher removal rates could only be obtained through an increase in laser power delivery.

Simulations revealed that material removal rates could be significantly enhanced by using a high repetition rate, high power femtosecond laser source and a redesigned CaF$_2$ objective. We determined that, for a given laser power, input fluences ~2–3 times the fluence threshold consistently produced the highest material removal rates when using a single fiber-based surgery probe. Further, material removal rates on the order of ~9 mm^3/min can be achieved through optimal selection of laser surgery parameters and through use of a fiber bundle. Additional studies are required to determine if simulated parameter sets are appropriate for ultrafast laser surgery of bone and whether bundle-fiber based probes can increase the ablation speed further. With future development, the surgical probe presented here can serve as a clinically viable tool for spinal decompression surgery.

Disclosures. Authors declare no conflict of interest.

Data availability. Datasets underlying the results presented in this paper are available in the Texas Data Repository [45].

References

1. J. L. Pao, W. C. Chen, and P. Q. Chen, "Clinical outcomes of microendoscopic decompressive laminotomy for degenerative lumbar spinal stenosis," Eur Spine J **18**(5), 672–678 (2009).

2. E. Burger, "Complications in spine surgery," Spine Trauma Surg. Tech. **13**, 399–403 (2010).
3. M. T. Espiritu, A. Rhyne, and B. V Darden, "Dural tears in spine surgery," American Academy of Orthopaedic Surgeon **18**(9), 537–545 (2010).
4. R. J. Mobbs, J. Li, P. Sivabalan, D. Raley, and P. J. Rao, "Outcomes after decompressive laminectomy for lumbar spinal stenosis: comparison between minimally invasive unilateral laminectomy for bilateral decompression and open laminectomy," J. Neurosurg. Spine **21**(2), 179–186 (2014).
5. A. Vogel, J. Noack, G. Hüttman, and G. Paltauf, "Mechanisms of femtosecond laser nanosurgery of cells and tissues," Appl. Phys. B **81**(8), 1015–1047 (2005).
6. J. Neev, L. B. Da Silva, M. D. Feit, M. D. Perry, A. M. Rubenchik, and B. C. Stuart, "Ultrashort pulse lasers for hard tissue ablation," IEEE J. Sel. Top. Quantum Electron. **2**(4), 790–800 (1996).
7. W. B. Armstrong, J. A. Neev, L. B. Da Silva, A. M. Rubenchik, and B. C. Stuart, "Ultrashort pulse laser ossicular ablation and stapedotomy in cadaveric bone," Lasers Surg. Med. **30**(3), 216–220 (2002).
8. B. Girard, D. Yu, M. R. Armstrong, B. C. Wilson, C. M. L. Clokie, and R. J. D. Miller, "Effects of femtosecond laser irradiation on osseous tissues," Lasers Surg. Med. **39**(3), 273–285 (2007).
9. Y. C. Lim, K. J. Altman, D. F. Farson, and K. M. Flores, "Micropillar fabrication on bovine cortical bone by direct-write femtosecond laser ablation," J. Biomed. Opt. **14**(6), 064021 (2009).
10. D. D. Lo, M. A. Mackanos, M. T. Chung, J. S. Hyun, D. T. Montoro, M. Grova, C. Liu, J. Wang, D. Palanker, A. J. Connolly, M. T. Longaker, C. H. Contag, and D. C. Wan, "Femtosecond plasma mediated laser ablation has advantages over mechanical osteotomy of cranial bone," Lasers Surg. Med. **44**(10), 805–814 (2012).
11. C. L. Hoy, N. J. Durr, P. Chen, W. Piyawattanametha, H. Ra, O. Solgaard, and A. Ben-Yakar, "Miniaturized probe for femtosecond laser microsurgery and two-photon imaging," Opt. Express **16**(13), 9996–10005 (2008).
12. C. L. Hoy, O. Ferhanoglu, M. Yildirim, W. Piyawattanametha, H. Ra, O. Solgaard, and A. Ben-Yakar, "Optical design and imaging performance testing of a 9.6-mm diameter femtosecond laser microsurgery probe," Opt. Express **19**(11), 10536–10552 (2011).
13. O. Ferhanoglu, M. Yildirim, K. Subramanian, and A. Ben-Yakar, "A 5-mm piezo-scanning fiber device for high speed ultrafast laser microsurgery," Biomed. Opt. Express **5**(7), 2023–2036 (2014).
14. T. Lanvin, D. B. Conkey, L. Descloux, A. Frobert, J. Valentin, J.-J. Goy, S. Cook, M.-N. Giraud, and D. Psaltis, "Ultrafast laser ablation for targeted atherosclerotic plaque removal," in Medical Laser Applications and Laser-Tissue Interactions VII, Lothar D. Lilge and Ronald Sroka, eds., *SPIE Proceedings* (Optical Society of America, 2015), Vol. 9542, p. 95420Z.
15. K. Subramanian, I. Gabay, O. Ferhanoğlu, A. Shadfan, M. Pawlowski, Y. Wang, T. Tkaczyk, and A. Ben-Yakar, "Kagome fiber based ultrafast laser microsurgery probe delivering micro-Joule pulse energies," Biomed. Opt. Express **7**(11), 4639–4653 (2016).
16. R. DeSalvo, A. A. Said, D. J. Hagan, E. W. Van Stryland, and M. Sheik-Bahae, "Infrared to ultraviolet measurements of two-photon absorption and n2 in wide bandgap solids," IEEE J. Quantum Electron. **32**(8), 1324–1333 (1996).
17. L. Gallais and M. Commandré, "Laser-induced damage thresholds of bulk and coating optical materials at 1030 nm, 500 fs," Appl. Opt. **53**(4), A186–A196 (2014).
18. L. Andrus and A. Ben-Yakar, "Thermal lensing effects and nonlinear refractive indices of fluoride crystals induced by high-power ultrafast lasers," Appl. Opt. **59**(28), 8806–8813 (2020).
19. H. Jeon, M. Pawlowski, L. P. Andrus, A. Ben-Yakar, and T. Tkaczyk, "Development of a miniature objective based on calcium fluoride and zinc sulfide lenses for ultrafast laser microsurgery applications (accepted June 2021)," *Opt. Eng.* (2021).
20. A. Ben-Yakar and R. L. Byer, "Femtosecond laser ablation properties of borosilicate glass," J. Appl. Phys. **96**(9), 5316–5323 (2004).
21. J. Krüger, D. Dufft, R. Koter, and A. Hertwig, "Femtosecond laser-induced damage of gold films," Appl. Surf. Sci. **253**(19), 7815–7819 (2007).
22. M. E. Shaheen, J. E. Gagnon, and B. J. Fryer, "Femtosecond laser ablation behavior of gold, crystalline silicon, and fused silica: a comparative study," Laser Phys. **24**(10), 106102 (2014).
23. S. Hell and E. H. K. Stelzer, "Properties of a 4Pi confocal fluorescence microscope," J. Opt. Soc. Am. A **9**(12), 2159–2166 (1992).
24. S. W. Hell, A. R. Utz, M. Schrader, P. E. Hänninen, and E. Soini, "Pulsed laser fluorophore deposition: a method for measuring the axial resolution in two-photon fluorescence microscopy," J. Opt. Soc. Am. A **12**(9), 2072–2076 (1995).
25. W. R. Zipfel, R. M. Williams, and W. W. Webb, "Nonlinear magic: multiphoton microscopy in the biosciences," Nat Biotechnol **21**(11), 1369–1377 (2003).
26. S. Preuss, A. Demchuk, and M. Stuke, "Sub-picosecond UV laser ablation of metals," Nat Biotechnol **61**(1), 33–37 (1995).
27. S. Nolte, C. Momma, H. Jacobs, A. Tünnermann, B. N. Chichkov, B. Wellegehausen, H. Welling, A. Tu, B. N. Chichkov, B. Wellegehausen, and H. Welling, "Ablation of metals by ultrashort laser pulses," J. Opt. Soc. Am. B **14**(10), 2716 (1997).
28. W. Kautek, J. Krüger, M. Lenzner, S. Sartania, C. Spielmann, and F. Krausz, "Laser ablation of dielectrics with pulse durations between 20 fs and 3 ps," Appl. Phys. Lett. **69**(21), 3146–3148 (1996).
29. J. Bonse, J. M. Wrobel, J. Krüger, and W. Kautek, "Ultrashort-pulse laser ablation of indium phosphide in air," Appl. Phys. A **72**(1), 89–94 (2001).

30. T. Q. Jia, Z. Z. Xu, X. X. Li, R. X. Li, B. Shuai, and F. L. Zhao, "Microscopic mechanisms of ablation and micromachining of dielectrics by using femtosecond lasers," Appl. Phys. Lett. **82**(24), 4382–4384 (2003).

31. V. Wieger, S. Zoppel, and E. Wintner, "Ultrashort pulse laser osteotomy," Laser Phys. **17**(4), 438–442 (2007).

32. L. T. Cangueiro, R. M. C. da, S. Vilar, A. M. B. do Rego, and V. S. F. Muralha, "Femtosecond laser ablation of bovine cortical bone," J. Biomed. Opt. **17**(12), 125005 (2012).

33. A. Rosenfeld, M. Lorenz, R. Stoian, and D. Ashkenasi, "Ultrashort-laser-pulse damage threshold of transparent materials and the role of incubation," Appl. Phys. A **69**(7), S373–S376 (1999).

34. J. He, Y. Qu, H. Li, J. Mi, and W. Ji, "Three-photon absorption in ZnO and ZnS crystals," Opt. Express **13**(23), 9235–9247 (2005).

35. B. Gu, J. He, W. Ji, and H.-T. Wang, "Three-photon absorption saturation in ZnO and ZnS crystals," J. Appl. Phys. **103**(7), 073105 (2008).

36. A. Vogel, N. Linz, S. Freidank, and G. Paltauf, "Femtosecond-laser-induced nanocavitation in water: implications for optical breakdown threshold and cell surgery," Phys. Rev. Lett. **100**(3), 038102 (2008).

37. Rüdiger Paschotta, *Field Guide to Laser Pulse Generation* (SPIE Press, 2008).

38. J. H. Marburger, "Self-focusing: theory," Prog. Quantum Electron. **4**, 35–110 (1975).

39. A. Brodeur and S. L. Chin, "Ultrafast white-light continuum generation and self-focusing in transparent condensed media," J. Opt. Soc. Am. B **16**(4), 637–650 (1999).

40. H. Urey, "Spot size, depth-of-focus, and diffraction ring intensity formulas for truncated Gaussian beams," Appl. Opt. **43**(3), 620–625 (2004).

41. E. Truumees, "Personal communication," (2021).

42. M. Werner, M. Klasing, M. Ivanenko, D. Harbecke, H. Steigerwald, and P. E. D.-V. Hering A, "CO_2 laser free form processing of hard tissue," in *Therapeutic Laser Applications and Laser-Tissue Interactions III, Proceedings of SPIE-OSA Biomedical Optics* (Optical Society of America, 2007), Vol. 6632, p. 6632_1.

43. K. Stock, R. Diebolder, F. Hausladen, and R. Hibst, "Efficient bone cutting with the novel diode pumped Er:YAG laser system: in vitro investigation and optimization of the treatment parameters," in *Proc. SPIE* (2014), Vol. 8926.

44. L. M. Beltrán Bernal, F. Canbaz, A. Droneau, N. F. Friederich, P. C. Cattin, and A. Zam, "Optimizing deep bone ablation by means of a microsecond Er:YAG laser and a novel water microjet irrigation system," Biomed. Opt. Express **11**(12), 7253–7272 (2020).

45. A. Ben-Yakar, "Bone Ablation Data for BOE 2021 paper," Texas Data Repository: Version 1, 2021, https://doi.org/10.18738/T8/T60MJI.